

# Light-travel-time diagnostics in early Supernova spectra: substantial mass loss of the IIb progenitor of SN 2013cu through a superwind

G. Gräfener<sup>1,2</sup> and J. S. Vink<sup>1</sup>

<sup>1</sup>Armagh Observatory, College Hill, Armagh, BT61 9DG, United Kingdom

<sup>2</sup>Argelander-Institut für Astronomie, Auf dem Hügel 71, 53121 Bonn, Germany

Received ; Accepted

## ABSTRACT

The progenitors of type-IIb supernovae (SNe) are believed to have lost their H-rich envelopes almost completely in the direct pre-SN phase. Recently the first “flash spectrum” of a SN IIb (SN 2013cu) has been presented, taken early enough to study its immediate circumstellar medium (CSM). Similar to a previous study by Groh (2014) we analyse the structure and chemical composition of the optically-thick CSM using non-LTE model atmospheres. For the first time we take light-travel time (LTT) effects on the spectrum formation into account, which affect the shapes and strengths of the observable emission lines, as well as the inferred SN luminosity. Based on the new CSM parameters we estimate a lower limit of  $\sim 0.3 M_{\odot}$  for the CSM mass, which is a factor 10–100 higher than previous estimates. The spectral fit implies a CSM in the form of a homogeneous and spherically symmetric superwind whose mass-loss rate exceeds common expectations by up to two orders of magnitude. The derived chemical composition is in agreement with a progenitor that has just left, or is just about to leave the Red-Supergiant (RSG) stage, confirming the standard picture for the origin of SNe IIb. Due to its extreme mass loss the SN progenitor will likely appear as extreme RSG, Luminous Blue Variable (LBV), or Yellow Hypergiant (YHG). The direct detection of a superwind, and the high inferred CSM mass suggest that stellar wind mass loss may play an important role in the formation of SNe IIb.

**Key words:** supernovae: general – supernovae: individual: SN 2013cu – stars: winds, outflows

## 1 INTRODUCTION

The question how massive stars end their lives is a fundamental question in Astrophysics, important for the understanding of the lifecycle of stars and the chemical enrichment of the interstellar medium throughout cosmic evolution. An important goal is to understand the connection between observed Supernova (SN) subtypes and their direct progenitors. Considerable progress in this direction has been made in the recent years through the direct identification of SN progenitors in pre-explosion images (cf. Smartt 2009). However, in many cases the unknown (and potentially peculiar) properties of direct SN progenitors substantially complicate the interpretation of the results (e.g. Yoon et al. 2012; Walmswell & Eldridge 2012; Gräfener et al. 2012).

With the recent advent of short-cadence transient surveys such as the intermediate Palomar Transient Survey (iPTF) a new window for the study of the connection between SNe and their direct progenitors has been opened. Early SN ‘flash’ spectroscopy, within about a day after explosion, allows the analysis of the direct environment of the SN and its progenitor before it is overrun by the SN shock front. The first example of such an observation, taken 15.5 h after explosion, has been presented for the type-IIb SN 2013cu (iPTF 13ast) by Gal-Yam et al. (2014), who interpreted the early

spectrum as a Wolf-Rayet (WR) type emission-line spectrum. Later Groh (2014) performed a detailed spectral analysis using the non-LTE model atmosphere code CMFGEN (Hillier & Miller 1998), and showed that the spectrum originates from a dense low-velocity wind or circum-stellar medium (CSM) that is more reminiscent of a Luminous Blue Variable (LBV) or Yellow Hypergiant (YHG) progenitor. Based on the abundances, mass-loss rate, and terminal wind velocity from this analysis Groh also predicted the possible spectral appearance of the progenitor.

The reason why the early spectrum of SN 2013cu appears similar to a stellar spectrum, albeit about 5 orders of magnitude brighter, is that the SN is still enshrouded in an optically thick wind/CSM, i.e., the SN shock front is not directly observed (Gal-Yam et al. 2014; Groh 2014). In such a case the spectrum formation is similar to the case of optically-thick stellar winds of WR stars or LBVs, whose emission-line spectra are dominated by recombination processes. Such objects obey scaling relations that preserve their optical depth scales and emission-line equivalent widths over large luminosity ranges (cf. Sect. 5.1 in Gräfener & Vink 2013). Despite the much lower densities in the spatially extended wind/CSM of SN 2013cu, its early spectral appearance is thus qualitatively similar to WR-type winds

with extremely low wind velocities, such as the ones discussed by [Gräfener & Vink \(2015\)](#), enabling a spectral analysis with methods traditionally used for the analysis of hot stars.

The presence of such a dense CSM is somewhat surprising, and possibly highly relevant for the formation scenario of SNe IIB. Evidence for the presence of winds/CSM around SNe IIB has been found previously from nebular H $\alpha$  ([Chugai 1991](#); [Patat et al. 1995](#); [Houck & Fransson 1996](#); [Maurer et al. 2010](#)), radio ([Fransson & Björnsson 1998](#); [Soderberg et al. 2006](#); [Kotak & Vink 2006](#)), and X-ray observations ([Soderberg et al. 2006](#); [Nymark et al. 2009](#); [Chevalier & Soderberg 2010](#)). The presence of a dense, and in some cases modulated CSM has been interpreted as the result of non-conservative binary interaction or modulated winds in binary systems ([Ryder et al. 2006](#)), or variable LBV-type mass loss through a strong stellar wind in the direct pre-SN stage ([Kotak & Vink 2006](#)). In the case of SNe IIB both forms of mass loss could be relevant for the removal of most of the H-rich outer layers of the progenitor, and thus for the weakness of hydrogen that characterises this type of SNe.

The binary scenario for the formation of SNe IIB is supported by low mass estimates for their progenitors, implying low wind mass-loss rates ([Woosley et al. 1994](#); [Hamuy et al. 2009](#); [Mazzali et al. 2009](#); [Silverman et al. 2009](#); [Bersten et al. 2012](#)) and the direct detection of possible binary partners at SN explosion sites ([Podsiadlowski et al. 1993](#); [Ryder et al. 2006](#); [Maund & Smartt 2009](#); [Folatelli et al. 2014](#); [Fox et al. 2014](#)). On the other hand the evidence for strong LBV-type mass loss in the direct pre-SN phase supports single star scenarios as the one presented by [Groh et al. \(2013a\)](#).

The early observations of SN 2013cu are providing for the first time the opportunity to analyse the immediate CSM of an SN IIB (progenitor) directly, to obtain further constraints on the above scenarios. In the present work we analyse the early emission-line spectrum of SN 2013cu with state-of-the-art model atmospheres (LTT), taking for the first time the influence of light-travel-time (LTT) effects into account (Sect. 3). From our quantitative spectroscopic analysis (Sect. 4) we obtain information about the structure, velocity, and chemical composition of the progenitors wind/CSM, providing information on the evolutionary status of the progenitor and the nature of its mass-loss (Sect. 5). Our conclusions are summarised in Sect. 6.

## 2 MODEL ASSUMPTIONS

In this section we describe the underlying model assumptions for the non-LTE spectral synthesis models used in this work. In Sect. 2.1 we summarise the model assumptions for our standard models, in Sect. 2.2 we discuss the relevant model parameters, and in Sect. 2.3 the numerical computation of the observable spectrum. Finally, in Sect. 2.4, we discuss the expected deviations from the standard model due to time dependent effects which may affect the spectrum formation in the direct CSM of early SNe.

The models used here have previously been used extensively for the modelling and spectral analysis of hot stars and their winds, in particular for stars with optically thick Wolf-Rayet type stellar winds.

### 2.1 Standard model atmospheres

The models presented here are model atmospheres simulating the

excitation conditions and the spectrum formation in the SN progenitors dense and optically thick wind. We assume that the SN is in a sufficiently early stage so that the SN shock, which is the source of the observed SN luminosity, is still located below the inner boundary of our model atmospheres at very large optical depth. In Sect. 5.1 we will discuss in more detail how this scenario applies to SN 2013cu. For our models the SN shock thus merely serves as a 'background' energy source which provides the observed photon flux. The created photons are diffusing through the dense wind material before they reach the lower boundary of our atmosphere models. Here we assume that this incident radiation field is well thermalised, and that the radiative flux stays constant within our model atmospheres, i.e., that the model atmospheres are in radiative equilibrium.

Our models are computed under standard assumptions for expanding atmospheres. These are spherical symmetry, stationarity, and homogeneity. The radiation field is computed in the co-moving frame of reference (CMF) following the method described by [Koesterke et al. \(2002\)](#). The atomic population probabilities  $n_i(r)$  are computed in non-LTE simultaneously with the radiation field under the assumption of statistical equilibrium (SE). The models take thousands of energy levels and millions of line transitions into account, taking advantage of the "super-level" approach (cf. [Gräfener et al. 2002](#)). The temperature structure is computed under the assumption of radiative equilibrium (RE) using the Unsoeld-Lucy type iteration scheme of [Hamann & Gräfener \(2003\)](#).

### 2.2 Model parameters

The models are defined by the radiative SN luminosity, and the structure and chemical composition of the CSM. The luminosity  $L_{\text{SN}}$  and inner-boundary radius  $R_{\text{SN}}$  of our models are connected with the core temperature  $T_{\text{SN}}$  via Stefan Boltzmann's law

$$L_{\text{SN}} = 4\pi R_{\text{SN}}^2 \sigma_{\text{SB}} T_{\text{SN}}^4. \quad (1)$$

We note that the inner boundary of our models is located at an (LTE-continuum) Rosseland optical depth  $\tau_{\text{R}} = 20$ , i.e.,  $T_{\text{SN}}$  may differ substantially from a classical effective temperature  $T_{\text{eff}}$ .  $T_{\text{eff}}$  is usually defined with respect to the radius  $R_{2/3}$  where  $\tau_{\text{R}} = 2/3$ . For the CSM from extended high-density stellar winds  $R_{2/3}$  can be much larger than  $R_{\text{SN}}$ .

The density  $\rho(r)$  and velocity  $v(r)$  throughout our models are assumed to originate from the homogeneous and stationary stellar wind of the SN progenitor, with a mass-loss rate  $\dot{M}$ . They are connected through the equation of continuity

$$\dot{M} = 4\pi \rho v r^2. \quad (2)$$

We further adopt a  $\beta$ -type velocity law of the form

$$v(r) = v_{\infty} \left(1 - \frac{r_0}{r}\right)^{\beta} \quad (3)$$

with the terminal velocity  $v_{\infty}$ , and connection radius  $r_0 \approx R_{\text{SN}}$ . The latter connects the outer velocity law with an exponential density structure at the inner boundary. We adopt  $\beta = 1/2$  throughout this work. The main purpose of the adopted velocity structure is to ensure high enough densities and optical depths to achieve local thermodynamic equilibrium (LTE) at the inner boundary of our models, i.e., in regions that are not directly observed. In Sects. 5.2 and 5.5 we will further discuss how the adopted velocity and density structure affects the interpretation of our results.

Finally, the chemical composition is given by mass fractions  $X_{\text{H}}$ ,  $X_{\text{He}}$ ,  $X_{\text{C}}$ ,  $X_{\text{N}}$ ,  $X_{\text{O}}$ ,  $X_{\text{Si}}$  and  $X_{\text{Fe}}$  of hydrogen, helium, carbon,

nitrogen, oxygen, silicon and the iron-group elements. The iron-group elements (Sc, Ti, V, Cr, Mn, Fe, Co, Ni) are combined in one generic model atom assuming relative solar abundances (cf. Gräfener et al. 2002). The detailed model atoms used in this work are identical to the ones from Gräfener & Hamann (2008). We further assume that all line profiles are intrinsically broadened with a Doppler velocity  $v_D = 10$  km/s due to micro-turbulence.

### 2.3 The formal integral

To compare the obtained models with observations their emergent spectra are computed in the observers frame. To this purpose the radiation field is computed ray-by-ray in a cartesian  $(p, z)$  coordinate system, where the  $z$ -coordinate is directed along each ray towards the observer, and  $p$  denotes the impact parameter perpendicular to  $z$ . These coordinates are connected to the radius via  $p^2 + z^2 = r^2$ .

Based on the obtained atomic population probabilities  $n_i(r)$  the emission and absorption coefficients  $\eta_\nu(p, z)$  and  $\kappa_\nu(p, z)$  are computed for each observers-frame frequency  $\nu$ , and the emergent intensity  $I_\nu(p)$  is integrated along each ray via

$$I_\nu(p) = \int_{-\infty}^{\infty} \eta_\nu e^{-\tau(p,z)} dz \quad (4)$$

where

$$\tau(p, z) = \int_z^{\infty} \kappa_\nu(p, z') dz'. \quad (5)$$

This formal integral includes further improvements over the previous CMF computation, including more complex atomic models with fine-structure splitting, and thermal frequency redistribution of photons due to free-electron scattering (cf. Hillier 1984).

### 2.4 Time dependence

In this section we wish to give a short overview of how time-dependent effects in transient systems may render the assumptions of the standard model, as outlined above, invalid.

Time dependence may affect our models in two ways. 1) A time-dependent radiation field may affect the SE and RE equations for which we assume stationarity in our models. As a result the obtained populations  $n_i(r)$  and temperatures  $T(r)$  may change. 2) Light-travel-time (LTT) effects may affect the radiative transfer, and thus change the internal and emergent radiation fields.

1) Time dependent terms in the SE and RE equations become important in cases where the radiation field changes faster (on timescale  $\tau_{\text{rad}}$ ) than individual atomic processes. Typically, the slowest processes involved in the spectrum formation are recombination processes, and it is important to test whether these are affected. 2) LTT effects become important when the dimensions of the spectrum-formation region are so large that the light-travel time  $\Delta r/c \gtrsim \tau_{\text{rad}}$ .

The fully time-dependent radiative transfer problem and its application for the spectrum formation in SNe is outlined by Hillier & Dessart (2012). However, in their practical computations also these authors set the time derivatives of the radiation field to zero, which is equivalent to the neglect of LTT effects. While this is justified for SN ejecta in later phases it will be problematic for early phases where  $\Delta r/c \gtrsim \tau_{\text{rad}}$ .

In this work we will concentrate specifically on the latter case and discuss the role of LTT effects on the spectrum formation in early SN CSM, while retaining the assumption of stationarity in

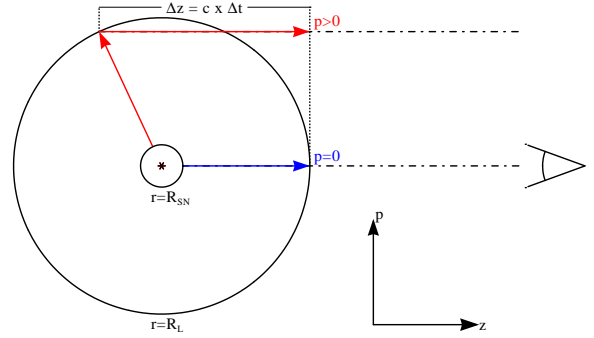


**Figure 1.** Computation of the time delay  $\Delta t$  on a radial shell with  $r = R_L$ . Indicated are two rays in the  $(p, z)$  coordinate system. The origin with  $p = z = r = 0$  is indicated by the asterisk. For the ray with  $p > 0$  (in red) the time delay originates from the indicated distance  $\Delta z = c \times \Delta t$  (cf. Eq. 6). For the central ray with  $p = 0$  and  $z = r$  (in blue)  $\Delta z = \Delta t = 0$ .

the SE and RE equations. This means that we compute the detailed atomic populations  $n_i(r)$  and the temperature  $T(r)$  in the usual manner, using stationary atmosphere models. Only in a second step, when the emergent spectrum is computed in the observers frame through Eq. 4, we take LTT effects into account. This approach is justified if  $\tau_{\text{rad}}$  is long enough to ensure a quasi-stationary state on a radial shell within the CSM that can be characterised by a single luminosity  $L_{\text{SN}}$ . In a first-order approximation, neglecting e.g. multiple scattering processes, such a shell (with a time-dependent radius  $R_L$ ) will move throughout the CSM with the speed of light  $c$ , and the  $n_i(R_L)$  and  $T(R_L)$  can be taken from a stationary model with the corresponding luminosity  $L$ .

## 3 LIGHT-TRAVEL-TIME EFFECTS

In this section we discuss the implementation of LTT effects in our models (Sect. 3.1), and their effects on the emergent fluxes and line profiles in early SN flash spectra (Sect. 3.2). As discussed above, such effects are expected to play a role for cases where the LTT throughout the CSM becomes comparable or larger than the timescale of the brightness variation  $\tau_{\text{rad}}$ .

As an example, for their early flash-spectrum of SN 2013cu Gal-Yam et al. (2014) estimated that the initial SN explosion took place  $t_{\text{exp}} = 15.5$  h before the spectrum was observed, i.e.,  $\tau_{\text{rad}} < 15.5$  h. On this timescale light travels  $R_{\text{exp}} = c \times t_{\text{exp}} \sim 1.7 \times 10^{15}$  cm  $\sim 24000 R_\odot$ . Radiation that is emitted at  $r = R_{\text{exp}}$  will thus only be visible for the observer if it stems from parts of the CSM that are directed towards us. The far side of the CSM is subject to a time delay  $\Delta t > t_{\text{exp}}$  corresponding to a time before the SN explosion.

Based on the r-band photometry from Gal-Yam et al. (2014) we estimate a brightness change of  $f_m \sim 1.7$  mag/day for the flash spectrum of SN 2013cu at the time of observation. In our model from Sect. 4.1 we adopt an inner boundary radius of  $2300 R_\odot$ , and an outer boundary radius of  $\sim 3 \times 10^5 R_\odot$ . The light-travel time  $t_{\text{LTT}}$  for these distances is 0.06 and 8 days respectively. We thus expect that spectral features which are formed in the outer portion of the CSM will be substantially affected by LTT effects.

### 3.1 Computation of the differential time delay $\Delta t$ and brightness change $\Delta m$

As outlined in Sect. 2.4 we assume that, at a given time  $t$ , the state of the CSM on a radial shell  $R_L$  can be described by a stationary model with luminosity  $L_{\text{SN}}$ . Furthermore we assume that  $R_L$  moves in radial direction with the speed of light  $c$ . In Fig. 1 we illustrate the light-travel paths in the  $(p, z)$  coordinate system for two rays with  $p = 0$  and  $p > 0$ . Only on the radial ray with  $p = 0$  and  $r = z$  (which is pointing directly towards the observer) the formal integral (Eq. 4) can be computed in the normal way. Because  $r = z$ ,  $R_L$  travels simultaneously with the light signal along the  $z$  axis. For all other rays with  $p > 0$  and  $r > z$  the LTT from a given radius  $r$  towards the observer is longer than for the central ray, by the distance  $\Delta z$  indicated in Fig. 1. The time difference is

$$\Delta t = \frac{\Delta z}{c} = \frac{1}{c} [r - z(p, r)] = \frac{1}{c} [r \pm \sqrt{r^2 - p^2}], \quad (6)$$

where the minus and plus signs in the last term correspond to the hemispheres directed towards and away from the observer respectively.

As a consequence the light that reaches the observer from an off-center ray with  $p > 0$  has been emitted earlier by a time delay  $\Delta t$ , compared to the light from the central ray with  $p = 0$ . We wish to emphasise that  $\Delta t$  is always positive. As long as the SN lightcurve is still rising this means that, compared to the central ray, all other rays have time delays  $\Delta t$  corresponding to times when the SN was fainter.

We further make the simplifying assumption that the spectrum emitted at  $t - \Delta t$  has the same spectral shape as the one at  $t = 0$ , except for being fainter by  $\Delta m = f_m \times \Delta t$ . Here  $f_m$  denotes the change in magnitude vs. time at the time of observation. Numerically this change is implemented by scaling the local emission coefficient  $\eta_\nu$  in Eq. 4 by a factor  $10^{-(2.5 \times \Delta m)}$ . We note that  $f_m$  characterises the brightness change in a specific wavelength range. In reality the spectral shape of the SN will change with time, and  $f_m$  will be a function of wavelength.  $f_m$  should thus be estimated for the same wavelength range in which the spectral modelling is performed.

As already indicated above, for early SNe before maximum LTT effects will always lead to a lower brightness than the one of the reference model with  $L_{\text{SN}}$ . This will particularly affect spectral features that originate from geometrical portions of the spectrum-emitting region with large time delays  $\Delta t$ . If also the continuum-emitting region is affected, LTT effects can even lead to a decrease of the observed continuum luminosity compared to the luminosity  $L_{\text{SN}}$  of the reference model. E.g., for our model in Sect. 4.1 we find that the classical photosphere is located at  $\sim 5 R_{\text{SN}}$ . The continuum emission thus originates from a spherical region beyond  $\pm 5 R_{\text{SN}}$ , i.e., with a spatial extension in  $z$  that is larger than  $10 R_{\text{SN}}$ . The corresponding time delay is of the order of 0.6 days, which implies that the continuum emission should be affected by LTT effects.

### 3.2 Theoretical line profiles

In Fig. 2 we present normalised theoretical line profiles from a CSM model for SN 2013cu with different adopted brightness changes  $f_m = 0.0$  (black), 1.7 (red), and 3.4 mag/day (blue). The model has been computed for a wind velocity of  $v_\infty = 103.7$  km/s. In our analysis in Sect. 4.1 the presented He I  $\lambda 5876$  line is the one which reacts strongest on LTT effects. The reason is that the line is formed at large radii far out in the CSM envelope (cf. Sect. 5.3). For this reason the unaffected line profile (with  $f_m = 0$ ) nearly displays

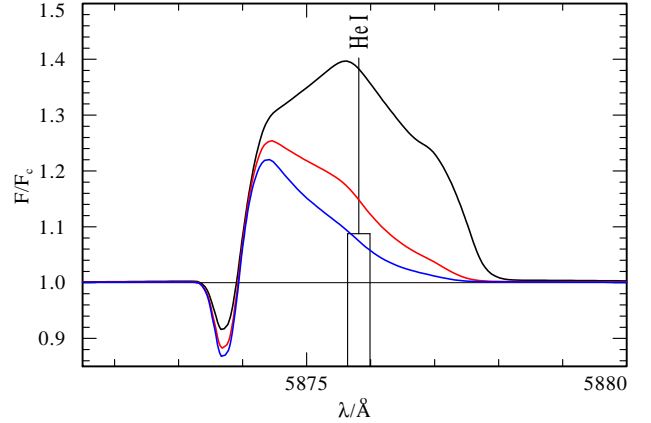


**Figure 2.** The influence of LTT effects on the He I  $\lambda 5876$  line profile. The presented normalised line profiles are computed for different adopted brightness changes  $f_m = 0.0$  (black), 1.7 (red), and 3.4 mag/day (blue).

a flat-top profile, as expected for optically thin emission from a hollow shell. However, owing to its small but finite optical depth, the line also shows a blue-shifted P-Cygni absorption feature at  $-\infty$ , and a moderate blue-red asymmetry due to internal absorption.

The influence of LTT effects, i.e. of an increased  $f_m$ , on the emergent spectrum are twofold. 1) As discussed in the previous section, the light from parts of the CSM that are farther away from the observer reaches the observer later, leading to an overall fainter spectrum, in particular also in the continuum. 2) The red line wings of emission lines in an expanding CSM are suppressed because they originate from the far side of the CSM which is moving away from the observer.

As demonstrated in Fig. 2 this effect has a strong influence on the normalised line profiles. For higher  $f_m$  we obtain weaker, narrower, and more blue-shifted line profiles with a stronger blue-red asymmetry. It is important to note that these effects are expected to affect lines with different formation depths differently, and will depend on the adopted value of  $v_\infty$ . We will discuss the additional diagnostic value of these LTT effects in Sect. 4.2 for the case of SN 2013cu.

## 4 THE FLASH SPECTRUM OF SN 2013CU

In Sect. 4.1 we present a quantitative spectral analysis of SN 2013cu. We note that a similar analysis has been presented previously by Groh (2014) without taking LTT effects into account. We will discuss the differences with respect to this work at a later stage in Sect. 5.2. In Sect. 4.2 we discuss the additional diagnostic value of LTT effects, followed by a detailed discussion of the observed H/He (Sect. 4.3) and metal line profiles (Sect. 4.4). The final model parameters and their dependence on the uncertain distance of SN 2013cu are discussed in Sect. 4.5.

### 4.1 Quantitative spectral analysis

Our analysis is based on the early flash spectrum of SN 2013cu as obtained by Gal-Yam et al. (2014) 15.5 hrs after explosion with the KECK DEep Imaging Multi-Object Spectrograph (DEIMOS) grating 600ZD, with a resolution of  $\sim 3.5 \text{ \AA}$  at  $7500 \text{ \AA}$  (corresponding to  $R \sim 2150$  or a broadening velocity of 140 km/s).



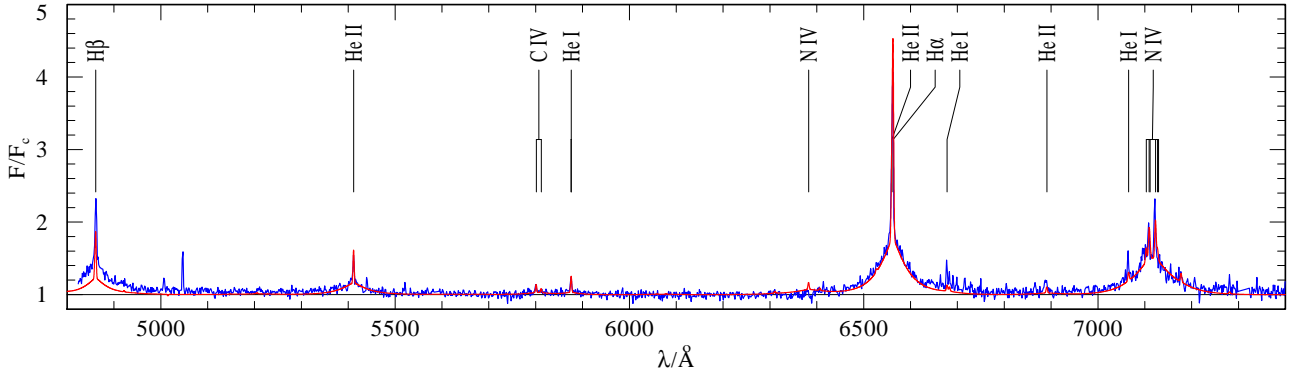


**Figure 3.** Spectral fit for the early flash spectrum of SN 2013cu, 15.5 hrs after explosion. Normalised spectrum of SN 2013cu (blue) with our best-fit model (red). After correction for redshift and extinction, observation and model have been normalised in the same way by division through the model continuum.

**Table 1.** Parameters for the CSM of SN 2013cu with rough fitting-errors where applicable.

CSM/wind parameters		mass fractions	
$\log(L_{\text{SN}}/L_{\odot})$	$10.47 \pm 0.05$	X	$0.25 \pm 0.1$
$\dot{M}/M_{\odot} \text{ yr}^{-1}$	$(4.9 \pm 0.3) \times 10^{-3}$	Y	$0.75 \pm 0.1$
$R_{\text{SN}}/R_{\odot}$	$4130 \pm 390$	Z	$0.007^{(c)}$
$T_{\text{SN}}/\text{kK}$	$37.2 \pm 1.3$	C	$4.0 \times 10^{-5(d)}$
$v_{\infty}/\text{km s}^{-1}$	$32.8^{(a)}$	N	$(3.9 \pm 1) \times 10^{-3}$
$v_{\text{D}}/\text{km s}^{-1}$	$10^{(b)}$	O	$2.5 \times 10^{-4(c)}$
$\beta$	$0.5^{(b)}$	Si	$3.3 \times 10^{-4(c)}$
		Fe <sup>(e)</sup>	$6.3 \times 10^{-4(c)}$
intrinsic model parameters			
$\log(L_{\text{SN}}/L_{\odot})$	10.0		
$\dot{M}/M_{\odot} \text{ yr}^{-1}$	$2.0 \times 10^{-3}$		
$R_{\text{SN}}/R_{\odot}$	2405		

The parameters in the upper part of this table are scaled values that are derived for an adopted distance of 108 Mpc. The systematic uncertainties arising from this assumption and the uncertain value of  $v_{\infty}$  are discussed in Sect. 4.5. The intrinsic model parameters are given in the lower part of the table for the parameters that differ from the scaled results. <sup>(a)</sup> This value represents a rough upper limit for  $v_{\infty}$  based on our discussion in Sects. 4.3 and 4.5. <sup>(b)</sup> Adopted value. <sup>(c)</sup> Indirect estimate based on the expected relative mass fractions of CNO processed material relative to the derived N abundance. <sup>(d)</sup> Same as (c) but in very good agreement with the observed strength of C IV  $\lambda 5801/12$ . <sup>(e)</sup> Combined mass fraction of Fe-group elements with relative abundances from Gräfener et al. (2002).

The data are publicly available at the Weizmann Interactive Supernova data REpository (WiSeREP, Yaron & Gal-Yam 2012). Following Gal-Yam et al. we scaled the spectral flux by 1.8 dex to match their observed host-subtracted photometry and H $\alpha$  line flux  $F_{\text{H}\alpha} = 3.4 \times 10^{-15} \text{ erg cm}^{-2} \text{ s}^{-1}$ . We further adopt the same distance of 108 Mpc, corresponding to a distance modulus  $m - M = 35.17$ , which is the luminosity distance towards the host galaxy UGC 9379 from the NASA Extragalactic Database (NED).

We initially started our analysis with the computation of a model grid neglecting LTT effects. Using this grid we could match the observed spectral energy distribution (SED) with a luminosity of  $10^{10} L_{\odot}$  (in very good agreement with the results of Groh 2014), and an extinction parameter of  $E(B - V) = 0.1$  using the standard Cardelli et al. (1988) extinction law with  $R_V = 3.1$ .

The following analysis is based on the same model grid, i.e.

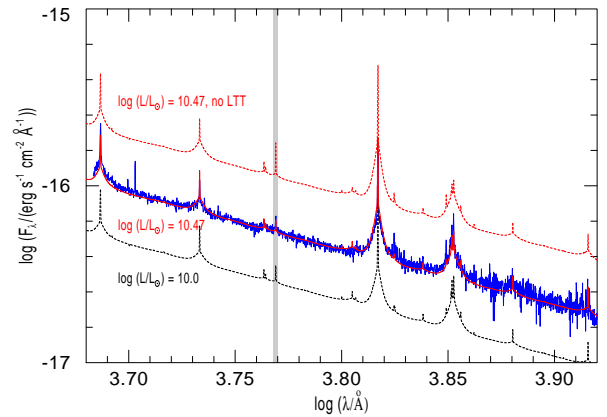


**Figure 4.** Spectral energy distribution (SED) of SN 2013cu compared to our models. Plotted are the observations in blue, and the SED of our best-fit model with LTT effects and  $L_{\text{SN}} = 10^{10} L_{\odot}$  in black, as well as test models with an increased luminosity of  $10^{10.47} L_{\odot}$  with and without LTT effects in red. Except for the differences in brightness the models show different strengths of He I  $\lambda 5876$  (highlighted in grey).

with a fixed luminosity of  $10^{10} L_{\odot}$ , but includes LTT effects. For the brightness change in the optical range we use a fixed value of  $f_m = 1.7 \text{ mag/day}$  as estimated from the r-band photometry of Gal-Yam et al. (2014).

In Fig. 3 we compare the synthetic line spectrum of our best-fit model with observations. To prevent ambiguities due to the normalisation procedure the observed spectrum has been normalised by dividing the de-reddened observation through the model continuum, scaled by a constant factor. While this model fits the observed line spectrum and the slope of the observed SED very well, the newly introduced LTT effects reduce the overall brightness (cf. Sect. 3.1), so that the model does not fit the SED in an absolute sense anymore. This is illustrated in Fig. 4 where we compare the SED of our models, with and without LTT effects, with the observed SED of SN 2013cu. Our model with  $10^{10} L_{\odot}$  lies now  $\sim 0.3$  dex below the observed SED. For conventional models such a discrepancy can be compensated very precisely with common scaling relations (cf. Sect. 4.5). In the present case, however, the inclusion of LTT effects introduces further changes in the line profiles and the scaling properties of the continuum (cf. Sect. 4.5). In our case these affect predominantly the strength of the He I features and degrade the fit quality with respect to the detailed model fits presented below. To

illustrate these effects we are plotting a test model with increased luminosity, with and without LTT effects, in Fig. 4.

The changes introduced by LTT effects complicate the analysis, and in particular the determination of the absolute luminosity, substantially. In view of the uncertain distance of the SN host galaxy UGC 9379 and our rather crude approximations concerning the inclusion of LTT effects, we decided to restrict our detailed line fit to models with a fixed luminosity of  $10^{10} L_{\odot}$  in this work, to keep the effort for the fitting procedure manageable. Only after a satisfactory line fit is obtained we will scale the obtained values of  $R_{\text{SN}}$  and  $\dot{M}$  to match the observed absolute continuum brightness in Sect. 4.5.

The line fit in Fig. 3 is obtained by adjusting the model parameters from Sect. 2.2 to match the diagnostic emission lines He II  $\lambda 5411$ , He I  $\lambda 5876$ , H $\alpha$ /He II  $\lambda 6562$ , C IV  $\lambda 5801/12$ , and N IV  $\lambda 7103-29$ . The core temperature  $T_{\text{SN}}$ , wind density  $\dot{M}/v_{\infty}$ , and H/He abundance ratio are determined via the three available diagnostic features of He II, He I, and H $\alpha$ /He II. When these quantities are fixed the trace element abundances of C and N can be determined from the C IV and N IV emission lines. The final model parameters are summarised in Tab. 1. We note that the listed parameters are the ones obtained after correction of  $L_{\text{SN}}$  for LTT effects and do not account for systematic differences that may arise from the scaling (cf. Sect. 4.5).

Unfortunately the derived C abundance is very uncertain as the strength of C IV depends strongly on  $T_{\text{SN}}$ . This leaves us in a situation where the only reliable metallicity indicator left is the N IV line. However, even within the large uncertainties, our models suggest an extremely low C/N ratio  $\lesssim 1/50 \dots 1/100$  by mass, implying that the observed material has been processed by the CNO cycle, and C and O have been almost completely transformed into N (cf. our discussion in Sect. 5.6). For our final model we thus decided to use the strength of the N IV line as a proxy for the total metallicity  $Z$ , and to adopt the relative abundances of C, N, O, Si and the Fe-group elements from an appropriate stellar evolution model with  $Z = Z_{\odot}$  from Ekström et al. (2012), i.e., to scale their absolute values with  $Z$  as the only free parameter.

So far we determined  $T_{\text{SN}}$ ,  $\dot{M}/v_{\infty}$ , and the mass fractions  $X$ ,  $Y$  and  $Z$  from the observed emission line strengths and the shape of the SED. Our synthetic spectrum in Fig. 3 reproduces the observed line profiles very well, including the strength of the diagnostic He I/He II lines, and the strong electron-scattering wings of H $\alpha$ , He II and N IV. This is a big improvement over the work of Groh (2014) who underestimated the electron-scattering wings and could not reproduce the observed He I features. On the downside the He I  $\lambda 6678$ , 7065 lines appear still too weak in our model, and we predict a weak N IV feature near 6383 Å which is not observed.

In the following we will further constrain the luminosity  $L_{\text{SN}}$ , and the terminal wind velocity  $v_{\infty}$ . As these values depend critically on LTT effects we continue here with a detailed discussion of LTT effects, specifically for the case of SN 2013cu. To this purpose we will have a close look on the narrow cores of the observed emission lines, and their detailed profiles. Only after  $L_{\text{SN}}$  and  $v_{\infty}$  are fixed we can obtain the mass-loss properties of the SN progenitor.

#### 4.2 The influence of LTT effects

In this section we discuss the specific influence of LTT effects on the flash spectrum of SN 2013cu, also to assess their additional diagnostic value on SN flash spectra in general. In analogy to Sect. 3.2 we adopt different brightness changes  $f_m = 0.0, 1.7$  and  $3.4$  mag/day and investigate their influence on the spectrum forma-

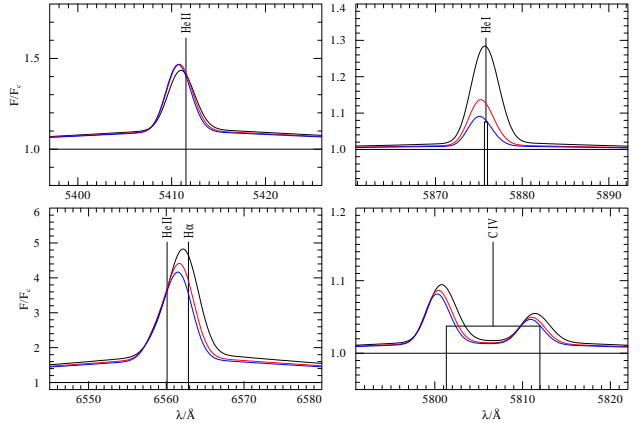


**Figure 5.** Theoretical line profiles for SN 2013cu assuming different brightness changes  $f_m = 0.0$  (black),  $1.7$  (red), and  $3.4$  mag/day (blue). A constant terminal wind velocity  $v_{\infty} = 103.7$  km/s is adopted for all models. The spectra are convolved with a Gaussian profile corresponding to an instrumental resolution of  $R = 2143$ , and a boxcar function corresponding to a wavelength sampling of  $1.5$  Å.

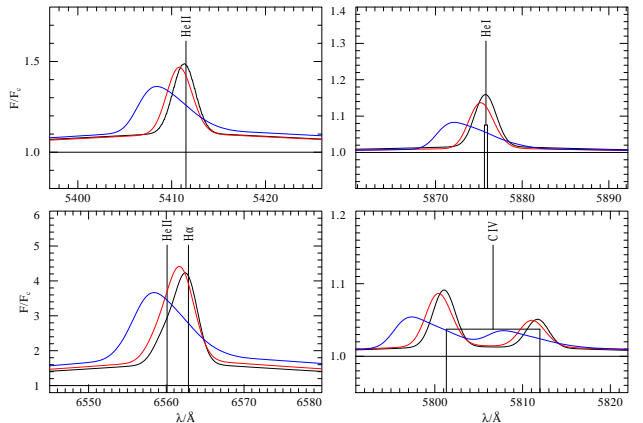


**Figure 6.** Same as Fig. 5 but for a model with fixed  $f_m = 1.7$  mag/day, and different terminal wind velocities  $v_{\infty} = 32.8$  (black),  $103.7$  (red), and  $328.0$  km/s (blue).

tion for our best-fit model from Sect. 4.1, which was obtained for  $f_m = 1.7$  mag/day. In particular, we also take the limited instrumental resolution and relatively coarse spectral sampling of the observations into account. To this purpose we convolve our theoretical spectrum with a Gaussian profile corresponding to an instrumental resolution of  $R = 2143$  and a boxcar function corresponding to a wavelength sampling of  $1.5$  Å.

As already discussed in Sect. 3.2 we find that, compared to a classical model with  $f_m = 0.0$ , our models including LTT effects are 1) fainter, and 2) show line profiles whose shapes are affected differently for each line. For the example of SN 2013cu we find substantial brightness reductions by factors of  $0.66$  for  $f_m = 1.7$ , and  $0.53$  for  $f_m = 3.4$  in the optical range. In our spectral analysis these effects will increase the derived luminosity roughly by a factor 2, which will also affect the derived size and density distribution of the CSM envelope.

The effects on the normalised emission-line profiles are shown in Fig. 5 for a model with a terminal wind velocity  $v_{\infty} = 103.7$  km/s.

Notably, in Fig. 5, He II  $\lambda 5411$  is hardly affected by the changes of  $f_m$  because this high-excitation line is formed near the center of the CSM envelope. On the other hand, lines that are formed in the outer part of the CSM, like He I  $\lambda 5876$ , are strongly affected. For these cases an increase of  $f_m$  leads to substantially weaker, narrower and blue-shifted line profiles. For the H $\alpha$ /He II  $\lambda 6562$  complex it appears that the He II component stays constant while H $\alpha$  is strongly affected. The C IV  $\lambda 5801/12$  doublet represents an intermediate case which is only moderately affected.

The above effects will alter the results of our spectral analysis in various ways. The change of the He I/He II ratio will affect the derived core temperature  $T_{\text{SN}}$ . However, as this ratio depends very sensitively on  $T_{\text{SN}}$ , the resulting changes are moderate. Moreover, the altered H $\alpha$ /He II ratio will affect the derived He abundance, while e.g. the derived C abundance will remain largely unaffected (the same holds for the N abundance based on N IV  $\lambda 7103-29$ ).

A very important effect of potentially high diagnostic value is introduced by the specific wavelength shifts and changes of the line widths of He I  $\lambda 5876$  and H $\alpha$ . While individual lines react differently on changes in  $f_m$ , the strength of the effect also depends on  $v_\infty$ . This is demonstrated in Fig. 6 where we compare models with different values of  $v_\infty$ . For this comparison the ratio  $\dot{M}/v_\infty$  has been kept fixed to ensure the same density distribution for all models. Otherwise all parameters are kept fixed as listed in Tab. 1. As to be expected it is clearly possible to distinguish between wind velocities of the order of 300 and 100 km/s as they are larger than the instrumental resolution. However, from Fig. 6 it appears that it may also be possible to identify line shifts below the instrumental resolution and to distinguish between terminal wind velocities of the order of 100 and 30 km/s. For observations with high enough S/N the line shifts introduced by LTT effects may thus present a new means to further constrain  $v_\infty$ , and thus the CSM properties from early SN observations like SN 2013cu.

### 4.3 Hydrogen and Helium line profiles

In Fig. 7 we compare the observed line profiles of the narrow emission-line cores of our three diagnostic H and He lines with models. In analogy to our comparison in Fig. 6 we compare the observations with two models with  $v_\infty = 32.8$  and 103.7 km/s and a fixed ratio  $\dot{M}/v_\infty$ . Furthermore, we adopt the standard brightness change of  $f_m = 1.7$  mag/day. As we obtain different intrinsic blueshifts for different values of  $v_\infty$  it was necessary to apply slightly different redshift corrections for the two different models.

The derived redshifts are mainly based on the velocity shift of He I  $\lambda 5876$ . In Fig. 8 we show  $\chi^2$ -fits for each line in Fig. 7 as a function of the adopted redshift correction  $v_{\text{rad}}$ . These help to quantify the fit quality and the relative line shifts for the models in Fig. 7.

For our model with  $v_\infty = 32.8$  km/s (left panels in Fig. 7, and black symbols in Fig. 8) we obtain a good match of the He I  $\lambda 5876$  profile simultaneously with the H $\alpha$ /He II blend with a redshift of  $v_{\text{rad}} = 7645$  km/s within  $\pm 5$  km/s. Compared to these two lines He II  $\lambda 5411$  may have a 10–20 km/s higher redshift. In particular, the synthetic H $\alpha$ /He II line profile matches the observation well, showing a similar asymmetry as observed.

For the model with  $v_\infty = 103.7$  km/s (right panels in Fig. 7 and red symbols in Fig. 8), the obtained fit quality of the H $\alpha$ /He II blend is worse, as supported by the higher  $\chi^2$  value in Fig. 8. The theoretical profile is symmetrical and does not match the observation very well. Furthermore the discrepancy between the line shift of He I  $\lambda 5876$  and He II  $\lambda 5411$  is larger than for our model with low  $v_\infty$ .

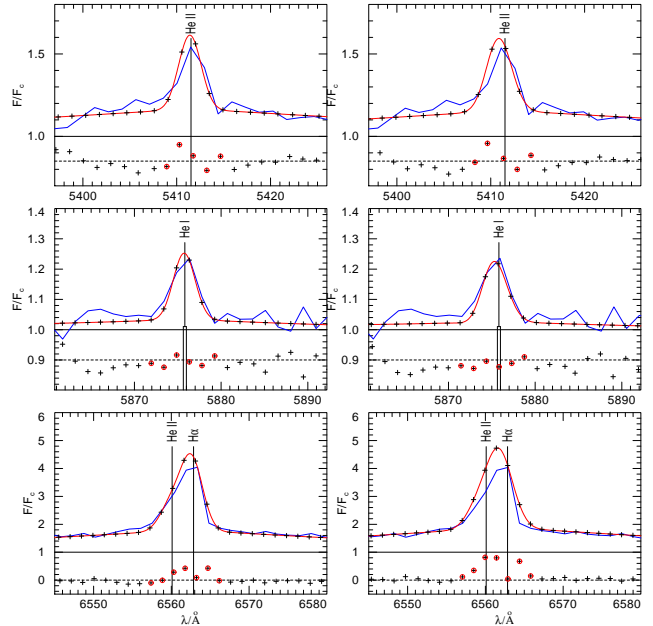


**Figure 7.** Comparison of observed H and He line profiles with models in the observers frame. The observed spectra (blue) are corrected for redshift to match the emission-line wavelengths as predicted by our models (red). Left panel: model with  $v_\infty = 32.8$  km/s and redshift 7645 km/s. Right panel: model with  $v_\infty = 103.7$  km/s and redshift 7665 km/s. Residuals are plotted at the bottom of each panel to indicate the fit quality (in some cases they are shifted along the y-axis). The residuals that are used for the  $\chi^2$  plot in Fig. 8 are encircled in red.

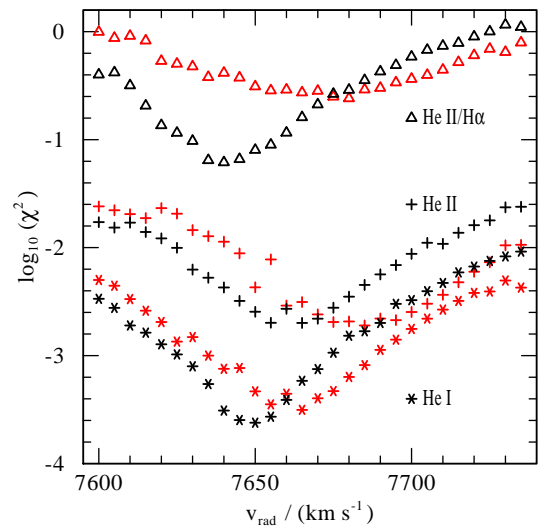


**Figure 8.**  $\chi^2$ -like merit function for the three diagnostic lines in Fig. 7, defined as the average of the square of the residuals over the line core (indicated by red circles in Fig. 7), vs. the adopted redshift  $v_{\text{rad}}$ . Black symbols indicate  $\chi^2$  for our model with  $v_\infty = 32.8$  km/s, red symbols for  $v_\infty = 103.7$  km/s.

The different symmetries of the theoretical H $\alpha$ /He II profiles are caused by LTT effects. While the intrinsic H $\alpha$ /He II profile is expected to be asymmetrical because of the different strengths of He II and H $\alpha$ , the asymmetry introduced by LTT effects (cf. Sect. 3.2) works in the opposite direction and lets the combined feature appear more symmetrical for higher wind velocities. For our model

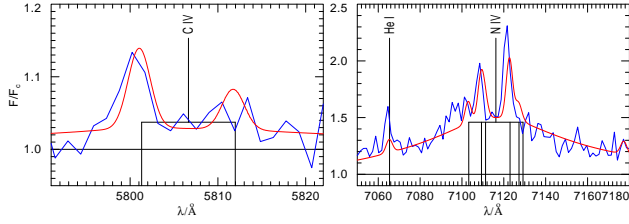


**Figure 9.** Comparison of observed C IV and N IV line profiles with our best-fit model ( $v_\infty = 32.8$  km/s). The same redshift as in Fig. 7 is applied.

with  $v_\infty = 103.7$  km/s these two effects appear to cancel each other, resulting in an almost symmetrical line profile. For our model with  $v_\infty = 32.8$  km/s the asymmetry due to LTT effects becomes smaller, and we obtain a line profile with a similar asymmetry as observed.

Due to the limited resolution of the present observations the effects discussed above are subtle, but we think that they are indicative of a terminal wind speed substantially lower than 100 km/s. Test computations with an intermediate value of  $v_\infty$  still favour the low value, i.e.,  $v_\infty \lesssim 32.8$  km/s. Lower values of  $v_\infty$  are difficult to assess 1) because of the limited resolution and S/N of the observations and 2) because of the adopted line broadening velocity of  $v_D = 10$  km/s in our models which introduces qualitative changes in the model structure for lower  $v_\infty$ .

We conclude that, if we take our predictions for LTT effects seriously, we favour a value of  $v_\infty \lesssim 32.8$  km/s. However, we note that this result may still be disputable, given the low S/N and coarse binning of the present observations. Based on the width of the observed line profiles alone we agree with Groh (2014) that values in excess of 100 km/s can be firmly excluded because of their substantial effect on the predicted line profiles (cf. Fig. 6).

#### 4.4 Metal lines

A detailed comparison of the observed and predicted C IV and N IV emission lines is shown in Fig. 9. While the theoretical line strengths and shapes of these features compare well with the observations, Fig. 9 reveals clear discrepancies in the absolute wavelengths. With respect to our synthetic line profiles the observed C IV doublet is blueshifted by  $\sim 30$  km/s, and the N IV multiplet by  $\sim 50$  km/s. The reason for this discrepancy is still enigmatic to us. The most likely reason is that the C and N ions experience a substantial radiative acceleration due to the intense radiation field of the SN explosion itself, and decouple from the rest of the plasma. This would explain why they are clearly blueshifted while nearby H and He lines appear unaffected. However, our discussion in Sect. 5.4 shows that, despite the extreme radiation field and the low density in the CSM, the conditions for ion-decoupling may be difficult to meet.

Particularly for the N IV multiplet it may also be possible that the wavelengths used in our model atom are incorrect. The wavelengths are obtained from the atomic database of the National Institute of Standards and Technology (NIST, Kramida et al. 2013), and are based upon purely theoretical level energies. On the other hand, similar discrepancies in the N IV wavelengths have never been reported before. Moreover, the C IV data for which the discrepancies are lower but still present are also obtained from NIST, but based on observed wavelengths. We thus think that ion-decoupling is a more plausible explanation.

#### 4.5 Final model parameters

As already outlined in Sect. 4.1 our previous analysis was based on a model with  $L_{\text{SN}} = 10^{10} L_\odot$  that does not match the absolute flux of SN 2013cu due to the newly introduced LTT effects. Our results thus need to be scaled to a higher value of  $L_{\text{SN}}$ .

For stars with strong stellar winds such scaling relations are well established (cf. Schmutz et al. 1989; Najarro et al. 1997; Hamann & Koesterke 1998; Gräfenner & Vink 2013). These relations are based on a scaling of  $R_{\text{SN}}$  and all involved spatial coordinates with a fixed core temperature  $T_{\text{SN}}$  so that  $L_{\text{SN}}$  follows from Eq. 1. In the time-dependent case such a scaling is further complicated by the dependence of LTT effects on  $\Delta r/c \times f_m$ . As the value of  $f_m$  is constrained by observations this means that an increase of  $L_{\text{SN}}$ , and thus  $\Delta r$ , leads to even stronger LTT effects so that  $L_{\text{SN}}$  needs to be increased even further.

As demonstrated in Fig. 4 our model with  $10^{10} L_\odot$  underpredicts the optical flux by  $\sim 0.3$  dex. Due to the non-linearity introduced by LTT effects we have to over-compensate this difference substantially, to match the absolute optical flux. If we also allow for a variation of the extinction coefficient we obtain satisfactory fits in the parameter range between ( $10^{10.42} L_\odot, E(B-V) = 0.05$ ) and ( $10^{10.50} L_\odot, E(B-V) = 0.10$ ). In Fig. 4 we show our best fit with ( $10^{10.47} L_\odot, E(B-V) = 0.07$ ), corresponding to an increased radial scale by a factor of  $\sim 1.7$ .

After correction of  $L_{\text{SN}}$  the obtained mass-loss rate has to be scaled with  $\dot{M} \propto L_{\text{SN}}^{3/4} \times v_\infty$  to ensure the preservation of the involved optical depth scales and relative emission line strengths (cf. Gräfenner & Vink 2013). The values of  $\dot{M}$  and  $R_{\text{SN}}$  after the scaling are given in the top panel of Tab. 1. In the scaled model the now much stronger LTT effects lead to a substantial reduction of the strength of He I  $\lambda 5876$ , i.e., to a degradation of the model fit (indicated by the grey shaded area in Fig. 4). Unfortunately, LTT effects thus introduce systematic uncertainties in our results that will most likely affect the derived H/He abundance and  $T_{\text{SN}}$ .

As the obtained value of  $L_{\text{SN}}$  also depends on the uncertain luminosity distance towards the SN host galaxy UGC 9379 we do not attempt to further improve the model fit and use the obtained parameters in the subsequent discussion as a function depending on the intrinsic luminosity  $L_{\text{SN}}$ .

$$\dot{M} = 4.9 \times 10^{-3} M_\odot \text{yr}^{-1} \times \left( \frac{L_{\text{SN}}}{10^{10.47} L_\odot} \right)^{\frac{4}{3}} \times \left( \frac{v_\infty}{32.8 \text{ km s}^{-1}} \right), \quad (7)$$

and

$$R_{\text{SN}} = 4130 R_\odot \times \left( \frac{L_{\text{SN}}}{10^{10.47} L_\odot} \right)^{\frac{1}{2}}. \quad (8)$$

## 5 DISCUSSION

In the following we discuss the implications of our results on the nature of the progenitor of SN 2013cu and its mass loss. After a discussion of the nature of SN 2013cu and our model assumptions in Sect. 5.1, we compare our results with previous works in Sect. 5.2. In Sect. 5.3 we estimate the properties of the ejected progenitor CSM, and in Sect. 5.4 we discuss whether our results are affected by the radiative acceleration of the SN explosion. Finally, we discuss the properties of the progenitors wind in Sect. 5.5, and its evolutionary state in Sect. 5.6.



### 5.1 SN 2013cu as interacting supernova

From the shape of the r-band lightcurve of SN 2013cu Gal-Yam et al. (2014) estimated an explosion time of 15.5 h before the flash spectrum from Sect. 4 was taken. At this time the SN was still about 2 mag below its r-band maximum around day 10, after which the r-band brightness declined smoothly by  $\sim 1$  mag up to day 30.

The fact that the early spectrum of SN 2013cu only shows narrow emission lines with their electron-scattering wings, and no sign of broad lines that are typically connected with SN ejecta, suggests that SN 2013cu is an interacting supernova. In this case the SN luminosity is created through interaction of the fast SN ejecta with the slow and optically thick wind/CSM of the progenitor. SNe of this type have been modeled e.g. by Moriya et al. (2011) and Dessart et al. (2015) whose simulations show that the observed luminosity is created in a thin shock layer that decelerates while travelling through the CSM.

Assuming an average velocity of  $10^4$  km/s such a shock would travel  $8.6 \times 10^{13}$  cm or  $1241 R_{\odot}$  per day. This distance is much smaller than the inner boundary radius of our models ( $R_{\text{SN}} \approx 4100 R_{\odot}$ ) and far below the location of the classical photosphere with  $\tau = 2/3$  which is located at  $R_{2/3} \sim 5.4 R_{\text{SN}}$ . In agreement with our model assumptions in Sect. 2.1 the thin SN shock will thus be located below  $R_{\text{SN}}$ , i.e. at very large optical depth, for several days after the SN explosion. Furthermore the shock will be located below the photosphere at  $R_{2/3}$  for  $\sim 2$  weeks.

The spectral evolution of SN 2013cu is in agreement with this picture. Gal-Yam et al. (2014) provided additional spectra around days 3, 6 and 69. Of these spectra the ones at days 3 and 6 show no sign of broad emission lines, while the spectrum at day 69 is clearly dominated by a SN spectrum of type IIb. This implies that around days 3 and 6 the SN shock was still located so far below  $R_{2/3}$  that it was not directly observable. On day 69, on the other hand, the SN ejecta travelled far beyond  $R_{2/3}$ , so that the CSM above the SN shock was optically thin. This late spectrum still shows narrow H $\alpha$  and [N II] emission that could be formed in the direct CSM, or alternatively, in a nearby H II region.

For our upcoming discussion of the observed CSM mass in Sect. 5.3 it is interesting whether the SN–CSM interaction in SN 2013cu ceased by day 69, as this could set a limit to the total CSM mass. The presence or absence of strong signs of interaction (cf. also Smith et al. 2010) depends on a variety of parameters, including the density of the CSM, the kinetic energy of the SN ejecta, and the optical depth of the CSM at the time of observation. According to Moriya et al. (2011) signs of interaction can be expected for mass-loss rates  $\dot{M} > 10^{-4} M_{\odot} \text{ yr}^{-1}$  (assuming  $v_{\infty} = 10$  km/s), which would put SN 2013cu just above the limit. As Moriya et al. used a high explosion energy of  $3 \times 10^{51}$  erg in their computations this limit could be higher for the case of SN 2013cu. Dessart et al. (2015) discussed how the line formation in interacting SNe depends on the location of the thin SN shock vs. the photospheric radius  $R_{2/3}$  and showed that, similar to what is observed for SN 2013cu, interacting SNe form line profiles with narrow components in earlier phases when  $R_{\text{shock}} < R_{2/3}$ , and with multiple (narrow and broad) components in late phases when  $R_{\text{shock}} < R_{2/3}$  and the CSM is optically thin. We think that it is presently not clear whether the two-component profiles in the late spectrum of SN 2013cu are a result of interaction or not.

In any case, based on a shock velocity of  $10^4$  km/s, an absence of interaction on day 69 would translate into a maximal extension of the CSM of  $\sim 86000 R_{\odot}$  or  $21 R_{\text{SN}}$ . This value is comparable to

the size of the He I line-forming region that we derive in Sect. 5.3 and would thus still be compatible with the CSM mass derived in this section.

Moreover, Moriya et al. (2011) showed that the end of the interaction phase, due to a limited spatial extension of the CSM, would result in a notable drop in brightness of the SN lightcurve. As the r-band photometry from Gal-Yam et al. (2014) up to day 30 does not show such drop, the SN–CSM interaction is most likely sustained at least until this date. Based on the same considerations as above this would indicate a minimum CSM extension of  $2.6 \times 10^{15}$  cm or  $\sim 9 R_{\text{SN}}$ . In any case, an analysis of the lightcurve beyond day 30 could give important clues on the spatial structure of the CSM and the mass-loss properties of the progenitor of SN 2013cu.

### 5.2 Comparison with previous results

The CSM parameters of SN 2013cu have been estimated previously by Gal-Yam et al. (2014) and Groh (2014). While Gal-Yam et al. used analytical estimates of the wind density based on the strength of H $\alpha$ , the analysis of Groh was based on detailed spectroscopic modelling very similar to the approach used in the present work. The main difference is that we take LTT effects into account, implying a higher luminosity by 0.47 dex and lower terminal wind velocity. If we adopt the same luminosity ( $\log(L_{\text{SN}}/L_{\odot}) = 10.0$ ) and wind velocity ( $v_{\infty} = 100$  km/s) as Groh we obtain a progenitor mass-loss rate of  $4.4 \times 10^{-3} M_{\odot} \text{ yr}^{-1}$  from Eq. 7, which compares well with the estimates of  $5 \times 10^{-3} M_{\odot} \text{ yr}^{-1}$  from Gal-Yam et al. (2014) and  $3 \times 10^{-3} M_{\odot} \text{ yr}^{-1}$  from Groh (2014), i.e., the results are largely consistent.

As already noted in Sect. 4.1 the spectral fit obtained in the present work is superior to the fit presented by Groh (2014) in two important aspects. 1) we are able to reproduce the strong electron-scattering wings of H $\alpha$ , He II and N IV very precisely and simultaneously with the narrow emission line cores of these lines, while Groh underpredicted the strength of the electron-scattering wings. 2) we are able to reproduce He I  $\lambda 5876$  and He II  $\lambda 5411$  simultaneously (with He I  $\lambda 6678$ , 7065 weaker than observed), while Groh could only reproduce He II, but no He I emission.

The electron-scattering wings are an important direct indicator of the density in the CSM as their strength scales linearly with the electron density. In comparison, the strength of the narrow emission-line cores scales with the square of the density because these lines are formed in emission-line cascades following (two-particle) recombination processes. In stellar winds the relative strength of these features is used to determine the degree of small-scale density inhomogeneities (clumping) within the wind (Hillier 1991; Hamann & Koesterke 1998). With respect to a homogeneous, spherically symmetric wind, any inhomogeneity increases the mean density ratio  $\langle \rho^2 \rangle / \langle \rho \rangle$ , and thus the ratio of the observable emissionline cores vs. their wings. The fact that we can reproduce both features simultaneously with a homogeneous wind model thus indicates that the CSM likely results from a homogeneous, spherically symmetric progenitor wind, and not from an inhomogeneous CSM as it may be expected e.g. for mass-loss due to non-conservative binary interactions.

The abundances derived in the present work are qualitatively similar to the ones obtained by Groh, in the sense that we find a CSM composition substantially enriched in He and N and depleted in C indicating material that has been processed by the CNO cycle. In our models we had to reduce the H-abundance to a mass fraction as low as  $X = 0.25$  to simultaneously reproduce the observed

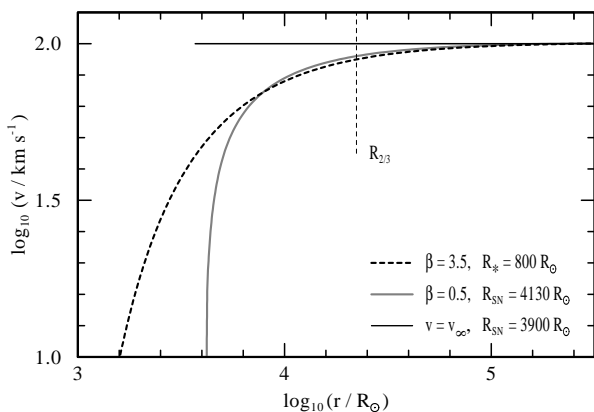


**Figure 10.** Comparison of our adopted velocity distribution with  $\beta = 0.5$  (grey) with other  $\beta$ -type velocity laws (black dashed line: slowly accelerating RSG wind with  $\beta = 3.5$ ; thin black line: constant-velocity CSM model from Groh (2014)). All examples are scaled to the same value of  $v_\infty = 100$  km/s.  $R_{2/3}$  indicates the photospheric radius with  $\tau = 2/3$ .

strengths of H $\alpha$ , He I and He II, while Groh derived a higher value of  $X = 0.46 \pm 0.2$ , just within the errorbars, without reproducing He I. Furthermore, our results are in agreement with a carbon mass fraction of  $X_C \approx 4.0 \times 10^{-5}$  which is four times higher than the value obtained by Groh, while our derived nitrogen mass fraction ( $X_N = (3.9 \pm 1) \times 10^{-3}$ ) is a factor two lower, indicating a sub-solar metallicity of  $Z \approx Z_\odot/2$ .

The differences between our work and the work of Groh are most likely caused by the different adopted velocity structures, in combination with the temperature sensitivity of the involved spectral features. While we use a standard  $\beta$ -type velocity law (Eq. 3) with  $\beta = 0.5$ , Groh used a constant velocity with an enhanced density at  $R_{SN}$  to mimic the presence of a thin shock. Both velocity structures are shown in Fig. 10. For a meaningful comparison we scaled the inner radius of the model of Groh using Eq. 1 to match the same value of  $L_{SN}$  as the one derived in this work.

First of all, Fig. 10 demonstrates that the resulting radii  $R_{SN}$  (and thus the core temperatures  $T_{SN}$  according to Eq. 1) are rather similar. The main difference lies in the velocity and density structure in the innermost part, near and below the photospheric radius  $R_{2/3}$ . At this radius our model displays lower velocities, and thus higher densities due to Eq. 2. Spectroscopically, the higher (electron) densities near and slightly below  $R_{2/3}$  will affect the strength of the electron-scattering wings which are formed in this region (cf. Sect. 5.3). The higher densities even further inside will not affect the emergent spectrum as these regions are located at large optical depths and are not directly observable.

The fact that the electron-scattering wings are better reproduced by our models can be seen as evidence for higher densities, and thus lower velocities near  $R_{2/3}$  than adopted by Groh (2014). This indicates a wind acceleration on a large radial scale. However, the fact that the region near  $R_{SN}$  is not directly observable also means that the derived value of  $R_{SN}$  will most likely not reflect the actual progenitor radius. In fact a radius of  $4100 R_\odot$  is much too large, even for the largest RSGs. Instead, the evidence for a slow acceleration near  $R_{2/3}$  should be interpreted as the result of a very slowly accelerating progenitor wind with a much smaller radius. This is illustrated in Fig. 10, by a velocity law with  $\beta = 3.5$  and  $R_* = 800 R_\odot$  that could represent a slowly accelerating RSG wind (cf. our discussion in Sect. 5.5). Alternatively, a time-dependent,

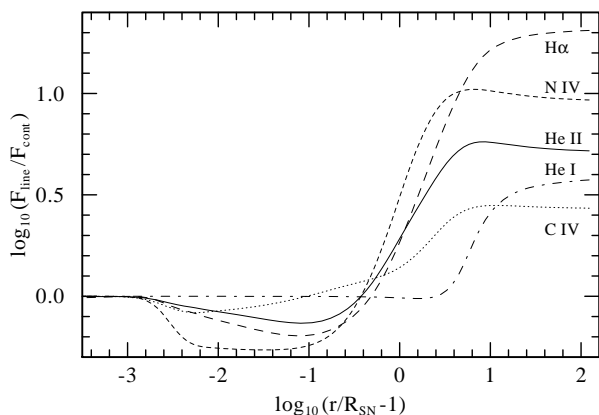


**Figure 11.** Ratio of line and continuum flux for our main diagnostic lines He II  $\lambda 5411$ , He I  $\lambda 5876$ , H $\alpha$ /He II  $\lambda 6562$ , C IV  $\lambda 5801/12$  and N IV  $\lambda 7103-29$  as an indicator of the line formation depth (see text).

slowly increasing mass-loss rate could be invoked to mimick a similar density structure.

### 5.3 Line-formation depth and CSM mass

The fact that our models reproduce the observed He I features, which are formed at very large radii, has important consequences for the derived minimum CSM mass and thus the mass-loss properties of the SN progenitor. To assess the amount of material that is directly observed via line emission we investigate in the following the formation depths of the diagnostic emission lines in our models.

To this purpose we extract CMF line fluxes from our models. In the CMF the profile shapes are qualitatively different from the observers frame. They consist of a line core near the central wavelength and a red-shifted line wing that can be either in emission or absorption. For our present models the extremum (i.e. either the maximum or minimum) of the line wing is located near a redshift of  $v_\infty$ . In Fig. 11 we plot the flux ratio between the extremum in the line wing ( $F_{line}$ ) and the continuum just blueward of the line core ( $F_{cont}$ ) as a function of radius. Most lines start with  $F_{line}/F_{cont} < 1$  at small radii, i.e., at small radii these lines are in absorption. Above this region  $F_{line}/F_{cont}$  increases until a saturation point with  $F_{line}/F_{cont} > 1$  is reached. We consider this point as the outer boundary of the formation region of the emission line. Beyond the saturation radius the line is passive and the line flux marginally decreases due to absorption.

From Fig. 11 it becomes clear that N IV is the line formed most deeply in the CSM envelope, followed by H $\alpha$  and He II. As the electron densities in the corresponding layers are high these lines have the strongest electron-scattering wings. Their formation region lies clearly below  $10 R_{SN}$ , i.e. near the classical photosphere with  $\tau = 2/3$  which is located at  $5.4 R_{SN}$  due to the extension of the CSM. The formation region of He I lies much further outward and ends at  $\sim 25 R_{SN}$ . With  $R_{SN}$  from Eq. 8 a continuous wind would need at least

$$25 R_{SN}/v_\infty = 69.5 \text{ yr} \times \left( \frac{L_{SN}}{10^{10.47} L_\odot} \right)^{\frac{1}{2}} \times \left( \frac{v_\infty}{32.8 \text{ km s}^{-1}} \right)^{-1} \quad (9)$$

to reach this radius. The total mass loss of the SN progenitor during

this time is

$$\dot{M} \times 25 R_{\text{SN}}/v_{\infty} = 0.34 M_{\odot} \times \left( \frac{L_{\text{SN}}}{10^{10.47} L_{\odot}} \right)^{\frac{1}{6}}. \quad (10)$$

We note that this value is a rough lower limit for the total mass-loss in the direct pre-SN stage as it only refers to the portion of the CSM which is observed directly. Owing to the larger size of the He I-emitting region compared to H $\alpha$ , and the higher luminosity the value derived here exceeds previous estimates by Gal-Yam et al. (2014); Groh (2014) by a factor 10 – 100.

#### 5.4 Radiative acceleration during the SN explosion

To prepare our discussion of the properties of the SN progenitor we examine here whether the radiative acceleration due to the SN explosion itself has an influence on the velocity field in the observed CSM. In our models the radiative acceleration is computed explicitly by integrating the product of opacity and flux in the CMF (cf. Gräfener & Hamann 2005). The resulting radiative acceleration can be written as

$$a_{\text{rad}} = \kappa_F \frac{F_{\text{rad}}}{c} = \kappa_F \frac{L_{\text{SN}}}{4\pi r^2 c}, \quad (11)$$

where  $F_{\text{rad}}$  denotes the radiative flux and  $\kappa_F$  the flux-weighted mean opacity.

For our present models  $a_{\text{rad}}$  turns out to be remarkably close (within 0.1 dex) to the value expected for pure electron scattering, i.e.,  $\kappa_F \approx \kappa_e = 0.2 \times (1 + X_{\text{H}}) \text{cm}^2 \text{g}^{-1}$ . With  $R_{\text{SN}}$  from Eq. 8 we thus obtain

$$a_{\text{rad}} \approx \kappa_e \frac{L_{\text{SN}}}{4\pi r^2 c} = \frac{26 \text{ km s}^{-1} \text{h}^{-1} (1 + X_{\text{H}})}{(r/R_{\text{SN}})^2}. \quad (12)$$

As the timescale  $\tau_{\text{rad}}$  is of the order of several hours we expect a substantial increase of the velocity near the inner boundary of our models (where  $r \approx R_{\text{SN}}$ ). However, due to the decline of  $a_{\text{rad}}$  with  $1/r^2$  the velocity increase is only of the order of few km/s near the photosphere (at  $r \approx 5 R_{\text{SN}}$ ) and negligible further out. In fact, there are signs of slight asymmetries in the electron-scattering wings in Figs. 7 and 9 that may originate from the additional acceleration in the deep sub-photospheric layers.

Another important aspect in this context is the possibility of ion decoupling, i.e., that complex ions experience a stronger radiative acceleration than H and He due to the larger number of absorbing spectral lines. If the radiative acceleration of these ions is strong enough to overcome Coulomb coupling they may separate from the H/He component of the plasma and show a distinct velocity field. In Sect. 4.4 we discussed that such an effect may indeed be observed for the C IV and N IV features in SN 2013cu.

A rough estimate of the importance of ion decoupling in a stellar wind is given by Lamers & Cassinelli (1999, Sect. 8.1.2). They find that the condition for the efficiency of Coulomb coupling depends on the ratio of luminosity over wind density via  $L v / \dot{M} \lesssim 5.9 \times 10^{16}$  (in  $L_{\odot} \text{ km s}^{-1} / M_{\odot} \text{ yr}^{-1}$ ). Using the parameters from Sect. 2.2 we obtain  $L v / \dot{M} \approx 1.5 \times 10^{14}$  which suggests that ion decoupling should not occur.

In any case, we do not expect that the narrow emission components of H and He are substantially affected, i.e., the velocities derived from these lines should be representative for the progenitor wind.

#### 5.5 Properties of the progenitor wind

From our previous analysis and discussion we obtained the following clues on the mass loss of the progenitor of SN 2013cu.

- 1) The strong and narrow emission-line cores suggest a high mass-loss rate of  $\sim 5 \times 10^{-3} M_{\odot} \text{ yr}^{-1}$  and low terminal wind velocity, possibly  $\lesssim 30 \text{ km/s}$ .
- 2) The strength of the electron-scattering wings suggests a homogeneous wind with a smooth density profile, that is accelerated on a large radial scale.
- 3) The size of the line-emitting region suggests that the wind was active over a period of at least 70 yr before the SN explosion, and that the mass lost during this period is  $\gtrsim 0.3 M_{\odot}$ .

First of all, the high mass-loss rate and large CSM mass indicate that the observed pre-SN mass loss may be relevant for the removal of the progenitor's H-envelope and thus for the formation of a SN of type IIb. In principle, a dense CSM could be formed in single star scenarios with strong stellar-wind mass loss in the direct pre-SN phase, or in binary scenarios with non-conservative mass transfer where a fraction of the H-envelope is expelled during the interaction process.

In the present case we think that the indications of homogeneity strongly support the stellar-wind scenario, because binary interaction scenarios would likely involve disk or spiral structures, i.e. large-scale inhomogeneities that would increase the ratio between the observed emission-line cores and their wings (cf. our discussion in Sect. 5.2). We thus think that the observed CSM has been ejected in the form of an extremely strong and slow continuous stellar wind.

For the mass-loss timescale we estimated a lower limit of several decades. In combination with the extremely high mass loss, this timescale is reminiscent of S-Doradus type variability with episodes of strong mass-loss, as it is observed for Luminous Blue Variables (LBVs) or Yellow Hypergiants (YHGs) (cf. Smith et al. 2004). Indications for this type of variable mass loss have also been found previously in radio lightcurves of transitional SNe (Kotak & Vink 2006). However, as the timescale derived in Eq. 9 is a lower limit, the observed pre-SN mass loss could also have occurred on a much longer timescale, including the possibility of a superwind at the end of the RSG phase (cf. Yoon & Cantiello 2010).

The low terminal wind speed in the CSM of SN 2013cu provides further hints on the nature of the progenitor because the mechanical energy of a stellar wind will be at least of similar order of magnitude as the energy that is needed to overcome the stellar gravitational potential, i.e.,  $v_{\infty} \gtrsim v_{\text{esc}}$ . Under this assumption the radius where the stellar wind is accelerated should be roughly of the order of

$$R_{\text{esc}} = \frac{2GM}{v_{\text{esc}}^2} = 4236 R_{\odot} \times \frac{M}{10 M_{\odot}} \times \left( \frac{v_{\text{esc}}}{30 \text{ km/s}} \right)^{-2}. \quad (13)$$

Notably, this value compares very well with our estimate of  $R_{\text{SN}}$  in Eq. 8, supporting the large radial scale of the wind acceleration in our models (cf. Fig. 10) in accordance with the observed strength of the electron-scattering wings (cf. our discussion in Sect. 5.2). Slow velocity laws such as the one with  $\beta = 3.5$  in Fig. 10 are found for some RSG winds (e.g. Baade et al. 1996; Bennett 2010).

However, also for hotter stars it may be possible to reduce  $R_{\text{esc}}$  substantially if the star is located near the Eddington limit. In this case the mass  $M$  in Eq. 13 may be substituted by  $M_{\text{eff}} = M(1 - \Gamma_e)$  where  $\Gamma_e = \kappa_e L / (4\pi c M G)$  is the classical Eddington factor due to free-electron scattering. In this way a low value of  $v_{\infty}$  would



point again towards LBV or YHG-like mass loss near the Eddington limit. In this case the smooth density structure could result from S Dor-type wind variability that would typically be expected to be of the order of decades.

What connects LBVs and YHGs with direct SN progenitors is their proximity to the Eddington limit (cf. Sect. 5.6). Enhanced mass loss near the Eddington limit has been subject of several theoretical and empirical studies, for the case of LBV's (Vink & de Koter 2002), and more recently for very massive stars (VMS) near the top of the main sequence (Gräfenor & Hamann 2008; Gräfenor et al. 2011; Vink et al. 2011; Vink & Gräfenor 2012; Bestenlehner et al. 2014). Owing to their proximity to the Eddington limit, it would be plausible that many direct SN progenitors exhibit similar mass-loss properties as these objects.

We conclude that the progenitor of SN 2013cu exhibited exceptionally strong mass loss over at least several decades in advance of the SN explosion. The wind properties point towards an unusually strong cool stellar wind, and/or an enhanced mass-loss rate due to the proximity to the Eddington limit. Based on the inferred wind properties we thus largely agree with (Groh 2014) who claimed that the SN progenitor had most likely similar spectroscopic/wind properties as LBVs or YHGs, except that we see no reason to exclude the possibility of an RSG progenitor with a cool superwind at the end of the RSG stage. In particular, we agree that the progenitor of SN 2013cu was not a WN star, as it was originally proposed by Gal-Yam et al. (2014).

### 5.6 Evolutionary status of the SNIb progenitor

The probably most important result of our analysis is that we confirm the standard picture for the origin of SNe Iib, namely that they are post-RSG objects that are almost entirely stripped off their H-rich envelope. This conclusion is based on the following arguments.

Despite the large uncertainties in the C abundance we can say that the observed value ( $X_C \approx 4 \times 10^{-5}$ ) is so low compared to the solar value ( $X_C = 2.3 \times 10^{-3}$ , Asplund et al. 2009) that carbon must have been destroyed in the CNO cycles. We can further conclude that the observed material is hardly mixed with unprocessed material, as this would drastically increase the C abundance. This is further supported by the high N/C ratio ( $X(N)/X(C) \approx 100$ ) which is in very good agreement with the CNO equilibrium value (cf. right panel of Fig. 3 in Arnould & Mowlavi 1993). Furthermore, the low H abundance ( $X = 0.25$ ) indicates that H-burning in the CNO-cycles is so advanced that also most of the initial O must have been transformed into N (cf. left panel of Fig. 3 in Arnould & Mowlavi 1993). This is further supported by the observed absolute N abundance ( $X_N = 3..5 \times 10^{-3}$ ), which is higher than the solar carbon abundance. We conclude that nitrogen most likely provides a very good proxy for the initial CNO abundance, and thus for the metallicity Z of the SN progenitor.

Based on the arguments above the observed composition likely resembles pure CNO-cycled material as it is found directly above the H-burning shell in RSGs (e.g. Fig. 2 in Georgy et al. 2014). In agreement with the standard scenario for SNe Iib the observed abundance pattern thus suggests that most of the H-rich envelope of the SN progenitor has been removed prior to explosion. An inspection of the evolutionary tracks of Ekström et al. (2012) reveals that only few models show a similar surface composition at the end of their evolution. In Tab. 2 we compare the stellar parameters of these models with our results (cf. also Groh et al. 2013b).

The three models have in common that they just left, or are just about to leave the RSG stage, i.e., they fit precisely in the

**Table 2.** Comparison between rotating and non-rotating single star progenitor models at carbon exhaustion from Ekström et al. (2012), and our results for SN 2013cu.

	rotating	non-rot.	non-rot.	SN 2013cu
$M_{\text{ini}}/M_{\odot}$	20	20	25	-
$M/M_{\odot}$	7.18	8.63	8.29	-
$\log(L/L_{\odot})$	5.28	5.18	5.38	-
$T_{\text{eff}}/K$	16053	3715	21218	-
$\dot{M}/10^{-5} \frac{M_{\odot}}{\text{yr}}$	1.2...15.3	2.9	0.98	490
X	0.24	0.48	0.16	0.24
Y	0.75	0.51	0.83	0.75
Z	0.014	0.014	0.014	0.007
X(C)	$7.9 \times 10^{-5}$	$1.0 \times 10^{-4}$	$8.7 \times 10^{-5}$	$4 \times 10^{-5}$
X(N)	$7.9 \times 10^{-3}$	$6.9 \times 10^{-3}$	$8.2 \times 10^{-3}$	$4 \times 10^{-3}$
X(O)	$5.0 \times 10^{-4}$	$1.6 \times 10^{-3}$	$1.1 \times 10^{-4}$	-
$\Gamma_e^{(a)}$	0.51	0.40	0.52	-

<sup>(a)</sup>  $\log(\Gamma_e) = \log(L/L_{\odot}) - \log(M/M_{\odot}) + \log(1+X) - 4.813$  for a fully ionised plasma.

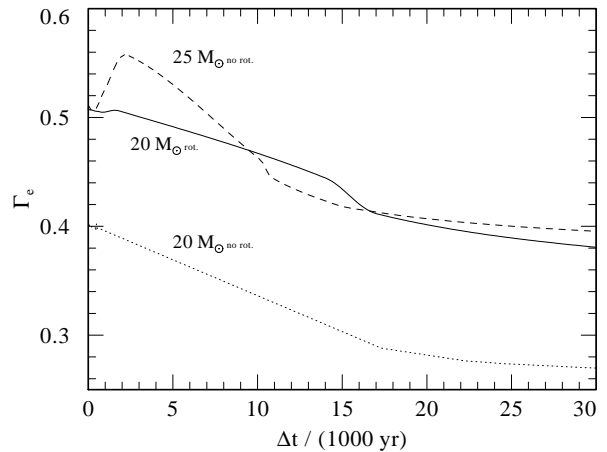


**Figure 12.** Eddington factor for a fully ionised plasma ( $\Gamma_e$ ) versus time before collapse ( $\Delta t$ ) for the three evolutionary models in Tab. 2.

standard picture of SNIb progenitors. Their Eddington factors ( $\Gamma_e$ ) are in the range 0.4-0.5. For hotter stars semi-empirical studies of Gräfenor et al. (2011); Bestenlehner et al. (2014) indicated a strong enhancement of stellar-wind mass loss in this parameter range (cf. also our discussion in Sect. 5.5). Furthermore, using the mass-loss recipes of Vink & de Koter (2002), Groh et al. (2013a) discussed the possible LBV nature of the rotating progenitor model with  $20 M_{\odot}$  from Tab. 2 based on its strong and variable mass loss. Notably, the final mass of this model ( $7.2 M_{\odot}$ ) is in agreement with mass estimates for the progenitor of the broad-lined type Iib SN 2003bg by Mazzali et al. (2009).

While the qualitative agreement of the observed abundance patterns with the evolutionary models in Tab. 2 is reassuring, it is important to note that our derived mass-loss rate exceeds expectations by roughly two orders of magnitude. If this type of superwind with its extreme mass loss would be persistent enough it may play an important role in the removal of the H-envelope in the direct pre-SN stages, and thus for the formation of SNe Iib, as well as stripped-envelope SNe Ibc.



The proximity to the Eddington limit could be a possible mechanism for triggering the enhanced mass loss. In Fig. 12 we show  $\Gamma_e$  for the evolutionary models in Tab. 2 as a function of time before collapse. Here  $\Gamma_e$  is computed for a fully ionised plasma (cf. note <sup>(a)</sup> in Tab 2). While this assumption holds well for the atmospheres of stars in excess of  $\sim 25000$  K, for cooler stars the given values would only be met in regions below the photosphere where the temperature is high enough to ionise H and He. All three models in Fig. 12 show an increase of  $\Gamma_e$  from about 15000 yr before collapse, which coincides with the time of He exhaustion in the core. If the observed mass loss is  $\Gamma_e$ -driven it could thus persist for several thousand years before collapse, i.e., much longer than the lower limit of  $\sim 70$  yr from Eq. 9. Consequently the total amount of ejected material could easily be of the order of several solar masses.

## 6 CONCLUSIONS AND OUTLOOK

In this work we analysed the properties of the direct CSM of SN 2013cu using a spectrum taken only 15.5 h after explosion. For the first time we investigated the impact of light-travel-time (LTT) effects on the spectrum formation in such an early SN stage.

We found that LTT effects affect the emergent spectra of early SNe (before they reach maximum brightness) in two ways. Firstly, the observable spectrum becomes fainter than expected without LTT effects. Secondly, the emission-line profiles become effectively narrower and blue-shifted depending on their formation depth, i.e., they change differently for different lines. These changes also affect the observable line strengths and line ratios. LTT effects thus provide additional diagnostic means for the quantitative analysis of early SN spectra.

The fact that LTT effects have substantial influence on the emergent spectrum and SED, means that they need to be included in quantitative spectroscopic studies of objects like SN 2013cu. In view of the involved observational uncertainties and theoretical simplifications, this unfortunately also means that potentially large systematic uncertainties arise. To get a better handle on the detailed time dependence it would be desirable to have high-quality high-cadence observations, and at the same time an improved numerical treatment of LTT effects.

Our present analysis of SN 2013cu leads to qualitatively similar results as previous works, but with some important quantitative differences.

We confirm the result of Groh (2014) that the SN progenitor was a star with a strong low-velocity wind, and not a high-velocity Wolf-Rayet wind as proposed by Gal-Yam et al. (2014). Mainly due to LTT effects we find a higher mass-loss rate, and indications for a lower wind velocity  $\lesssim 30$  km/s. From our improved fit of the strong electron-scattering wings we further conclude that the CSM is likely homogeneous and spherically symmetric, with a density gradient that varies slowly on a large radial scale of several thousand  $R_\odot$ . These results could indicate a strong cool RSG-like stellar wind, but could also be interpreted as LBV or YHG-like mass-loss as previously proposed by Groh (2014). In any case the observed mass loss is exceptionally high, up to two orders of magnitude higher than what is adopted in current stellar evolution models.

We further confirm the result of Groh (2014) that the CSM is deficient in hydrogen and carbon, and enriched in nitrogen, as expected for CNO-processed material. From our improved fit of the H, He I, He II, C IV, and N IV lines we derive a lower H abundance and possibly higher C abundance, in very good agreement with expectations for pure (un-mixed), almost fully CNO-processed ma-

terial. Such a composition is predicted for regions directly above the H-burning shell in RSGs, i.e., it confirms the standard picture that SNe IIB are formed from progenitors whose H-envelopes are almost entirely removed. This may include RSGs at the end of the RSG phase, or objects that have just left the RSG stage, with a spectroscopic appearance similar to LBVs or YHGs.

Mainly because of the indications for homogeneity from the precise fit of the observed electron-scattering wings we believe that the observed CSM has most likely been formed by a strong superwind, and not through mass loss in a scenario with non-conservative binary interaction. This could indicate that at least a part of the SNe IIB is formed in a single star scenario with strong mass loss in the direct pre-SN stage.

Based on the size of the He I-emitting region we deduce an observed CSM mass of  $\sim 0.3 M_\odot$  which is a factor 10 – 100 higher than previous estimates based on H $\alpha$ . This value poses a lower limit to the mass lost by the progenitor in the direct pre-SN stage. Based on the estimated mass-loss rate this corresponds to a period of strong mass-loss longer than roughly 70 yr before explosion. We argue that the occurrence of the exceptionally strong mass loss could be connected to the proximity of the SN progenitor to the Eddington limit, and the true CSM mass could be substantially higher than the derived lower limit.

In the future, an increasing number of early SN observations will hopefully provide a broader database to examine the properties of direct SN progenitors, and thus help to connect our understanding of stellar evolution with the observed types of SNe. Here we have shown that LTT effects may provide additional diagnostic means for the quantitative interpretation of these upcoming observations. In the present case we were mainly limited by the low spectral resolution and S/N of the observations. Moreover, we think that the theoretical modelling would benefit from a better time coverage with a cadence of few hours, to get a better handle on the time dependence of the spectrum.

## ACKNOWLEDGMENTS

We thank the referee, Jose Groh, for his comments that helped to greatly improve the manuscript. Furthermore we thank T. Moriya, T.-W. Chen, and R. Kotak for their helpful tips. This work was funded by the STFC under grant No. ST/J001082/1, and the Department of Culture, Arts and Leisure in Northern Ireland. This research has made use of the NASA/IPAC Extragalactic Database (NED) which is operated by the Jet Propulsion Laboratory, California Institute of Technology, under contract with the National Aeronautics and Space Administration.

## REFERENCES

- Arnould M., Mowlavi N., 1993, in Weiss W. W., Baglin A., eds, *Astronomical Society of the Pacific Conference Series Vol. 40, IAU Colloq. 137: Inside the Stars*. pp 310–323
- Asplund M., Grevesse N., Sauval A. J., Scott P., 2009, *ARA&A*, **47**, 481
- Baade R., Kirsch T., Reimers D., Toussaint F., Bennett P. D., Brown A., Harper G. M., 1996, *ApJ*, **466**, 979
- Bennett P. D., 2010, in Leitherer C., Bennett P. D., Morris P. W., Van Loon J. T., eds, *Astronomical Society of the Pacific Conference Series Vol. 425, Hot and Cool: Bridging Gaps in Massive Star Evolution*. p. 181 ([arXiv:1004.1853](https://arxiv.org/abs/1004.1853))
- Bersten M. C., et al., 2012, *ApJ*, **757**, 31
- Bestenlehner J. M., et al., 2014, *A&A*, **570**, A38

- Cardelli J. A., Clayton G. C., Mathis J. S., 1988, *ApJ*, 329, L33
- Chevalier R. A., Soderberg A. M., 2010, *ApJ*, 711, L40
- Chugai N. N., 1991, *MNRAS*, 250, 513
- Dessart L., Audit E., Hillier D. J., 2015, *MNRAS*, 449, 4304
- Ekström S., et al., 2012, *A&A*, 537, A146
- Folatelli G., et al., 2014, *ApJ*, 793, L22
- Fox O. D., et al., 2014, *ApJ*, 790, 17
- Fransson C., Björnsson C.-I., 1998, *ApJ*, 509, 861
- Gal-Yam A., et al., 2014, *Nature*, 509, 471
- Georgy C., Saio H., Meynet G., 2014, *MNRAS*, 439, L6
- Gräfener G., Hamann W.-R., 2005, *A&A*, 432, 633
- Gräfener G., Hamann W.-R., 2008, *A&A*, 482, 945
- Gräfener G., Vink J. S., 2013, *A&A*, 560, A6
- Gräfener G., Vink J. S., 2015, *A&A*, 578, L2
- Gräfener G., Koesterke L., Hamann W.-R., 2002, *A&A*, 387, 244
- Gräfener G., Vink J. S., de Koter A., Langer N., 2011, *A&A*, 535, A56
- Gräfener G., Owocki S. P., Vink J. S., 2012, *A&A*, 538, A40
- Groh J. H., 2014, *A&A*, 572, L11
- Groh J. H., Meynet G., Ekström S., 2013a, *A&A*, 550, L7
- Groh J. H., Meynet G., Georgy C., Ekström S., 2013b, *A&A*, 558, A131
- Hamann W.-R., Gräfener G., 2003, *A&A*, 410, 993
- Hamann W.-R., Koesterke L., 1998, *A&A*, 335, 1003
- Hamuy M., et al., 2009, *ApJ*, 703, 1612
- Hillier D. J., 1984, *ApJ*, 280, 744
- Hillier D. J., 1991, *A&A*, 247, 455
- Hillier D. J., Dessart L., 2012, *MNRAS*, 424, 252
- Hillier D. J., Miller D. L., 1998, *ApJ*, 496, 407
- Houck J. C., Fransson C., 1996, *ApJ*, 456, 811
- Koesterke L., Hamann W.-R., Gräfener G., 2002, *A&A*, 384, 562
- Kotak R., Vink J. S., 2006, *A&A*, 460, L5
- Kramida A., Ralchenko Y., Reader J., the NIST ASD Team 2013, NIST Atomic Spectra Database (ver. 5.1), <http://physics.nist.gov/asd>, National Institute of Standards and Technology, Gaithersburg, MD.
- Lamers H. J. G. L. M., Cassinelli J. P., 1999, *Introduction to Stellar Winds*. Cambridge University Press
- Maud J. R., Smartt S. J., 2009, *Science*, 324, 486
- Maurer I., Mazzali P. A., Taubenberger S., Hachinger S., 2010, *MNRAS*, 409, 1441
- Mazzali P. A., Deng J., Hamuy M., Nomoto K., 2009, *ApJ*, 703, 1624
- Moriya T., Tominaga N., Blinnikov S. I., Baklanov P. V., Sorokina E. I., 2011, *MNRAS*, 415, 199
- Najarro F., Hillier D. J., Stahl O., 1997, *A&A*, 326, 1117
- Nymark T. K., Chandra P., Fransson C., 2009, *A&A*, 494, 179
- Patat F., Chugai N., Mazzali P. A., 1995, *A&A*, 299, 715
- Podsiadlowski P., Hsu J. J. L., Joss P. C., Ross R. R., 1993, *Nature*, 364, 509
- Ryder S. D., Murrowood C. E., Stathakis R. A., 2006, *MNRAS*, 369, L32
- Schmutz W., Hamann W.-R., Wessolowski U., 1989, *A&A*, 210, 236
- Silverman J. M., Mazzali P., Chornock R., Filippenko A. V., Clocchiatti A., Phillips M. M., Ganeshalingam M., Foley R. J., 2009, *PASP*, 121, 689
- Smartt S. J., 2009, *ARA&A*, 47, 63
- Smith N., Vink J. S., de Koter A., 2004, *ApJ*, 615, 475
- Smith N., Chornock R., Silverman J. M., Filippenko A. V., Foley R. J., 2010, *ApJ*, 709, 856
- Soderberg A. M., Chevalier R. A., Kulkarni S. R., Frail D. A., 2006, *ApJ*, 651, 1005
- Vink J. S., Gräfener G., 2012, *ApJ*, 751, L34
- Vink J. S., de Koter A., 2002, *A&A*, 393, 543
- Vink J. S., Muijres L. E., Anthonisse B., de Koter A., Gräfener G., Langer N., 2011, *A&A*, 531, A132
- Walmswell J. J., Eldridge J. J., 2012, *MNRAS*, 419, 2054
- Woosley S. E., Eastman R. G., Weaver T. A., Pinto P. A., 1994, *ApJ*, 429, 300
- Yaron O., Gal-Yam A., 2012, *PASP*, 124, 668
- Yoon S.-C., Cantiello M., 2010, *ApJ*, 717, L62
- Yoon S.-C., Gräfener G., Vink J. S., Kozyreva A., Izzard R. G., 2012, *A&A*, 544, L11